Article

Developmental Cell

Actin Filament Turnover Drives Leading Edge Growth during Myelin Sheath Formation in the Central Nervous System

Graphical Abstract

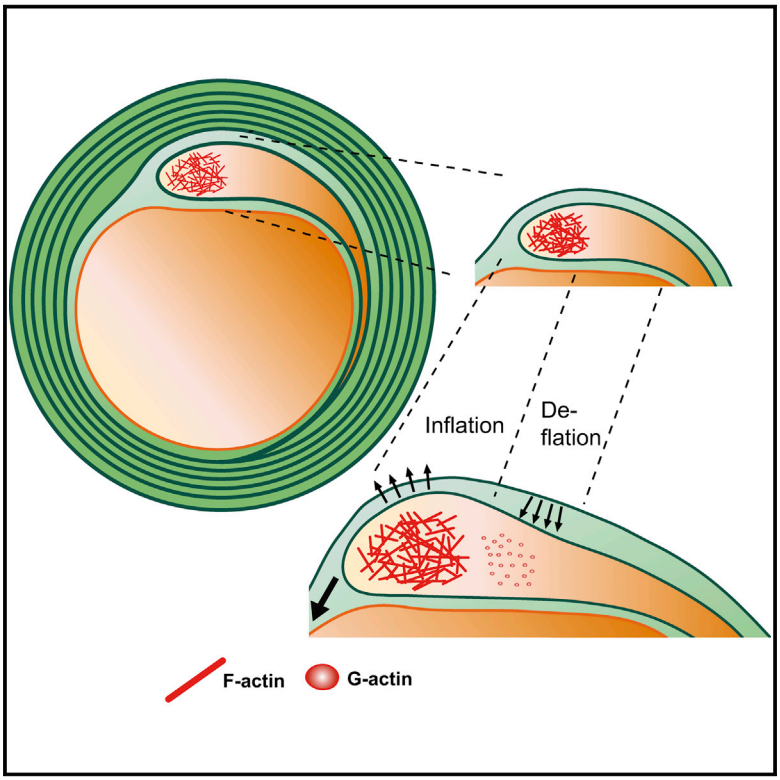

Authors

Schanila Nawaz, Paula Sánchez, Sebastian Schmitt, ..., Iwan A.T. Schaap, David A. Lyons, Mikael Simons

Correspondence

msimons@gwdg.de

In Brief

Oligodendrocytes wrap their plasma membrane around axons to generate multilamellar myelin sheaths, but the molecular machinery that drives growth has not been identified. Nawaz and Sánchez et al. show that F-actin turnover is the driving force in myelin wrapping by regulating repetitive cycles of leading edge protrusion and spreading.

Highlights

- F-actin is redistributed to the leading edge of the myelin sheath during growth
- Oligodendrocytes exhibit an adhesion-independent mode of leading edge protrusion
- F-actin depolymerization reduces tension and triggers myelin sheet growth
- ADF/cofilin1 activity drives myelin wrapping by maintaining high F-actin turnover

Nawaz et al., 2015, Developmental Cell *34*, 139–151
July 27, 2015
http://dx.doi.org/10.1016/j.devcel.2015.05.013

CellPress

Developmental Cell
Article

Actin Filament Turnover Drives Leading Edge Growth during Myelin Sheath Formation in the Central Nervous System

Schanila Nawaz,[1,2,8] Paula Sánchez,[1,2,3,7,8] Sebastian Schmitt,[1,2] Nicolas Snaidero,[1,2] Mišo Mitkovski,[1] Caroline Velte,[1,2] Bastian R. Brückner,[4] Ioannis Alexopoulos,[1] Tim Czopka,[5] Sang Y. Jung,[1] Jeong S. Rhee,[1] Andreas Janshoff,[4] Walter Witke,[6] Iwan A.T. Schaap,[3,7] David A. Lyons,[5] and Mikael Simons[1,2,*]
[1]Max Planck Institute for Experimental Medicine, 37075 Göttingen, Germany
[2]Department of Neurology, University of Göttingen, 37075 Göttingen, Germany
[3]Physics Institute, Faculty of Physics, University of Göttingen, 37077 Göttingen, Germany
[4]Institute for Physical Chemistry, University of Göttingen, 37075 Göttingen, Germany
[5]Centre for Neuroregeneration, Chancellor's Building, GU 507B, 49 Little France Crescent, Edinburgh EH16 4SB, UK
[6]Institute of Genetics, University of Bonn, Karlrobert-Kreiten Strasse 13, 53115 Bonn, Germany
[7]Center for Nanoscale Microscopy and Molecular Physiology of the Brain (CNMPB), 37073 Göttingen, Germany
[8]Co-first author
*Correspondence: msimons@gwdg.de
http://dx.doi.org/10.1016/j.devcel.2015.05.013

SUMMARY

During CNS development, oligodendrocytes wrap their plasma membrane around axons to generate multilamellar myelin sheaths. To drive growth at the leading edge of myelin at the interface with the axon, mechanical forces are necessary, but the underlying mechanisms are not known. Using an interdisciplinary approach that combines morphological, genetic, and biophysical analyses, we identified a key role for actin filament network turnover in myelin growth. At the onset of myelin biogenesis, F-actin is redistributed to the leading edge, where its polymerization-based forces push out non-adhesive and motile protrusions. F-actin disassembly converts protrusions into sheets by reducing surface tension and in turn inducing membrane spreading and adhesion. We identified the actin depolymerizing factor ADF/cofilin1, which mediates high F-actin turnover rates, as an essential factor in this process. We propose that F-actin turnover is the driving force in myelin wrapping by regulating repetitive cycles of leading edge protrusion and spreading.

INTRODUCTION

Information processing in complex organisms requires fast nerve transmission, which is achieved by the ensheathment of axons with myelin (Sherman and Brophy, 2005; Fields, 2008). The formation of myelin represents one of the most striking morphological transitions of a plasma membrane observed in an organism (Bauer et al., 2009; Simons and Lyons, 2013; Bercury and Macklin, 2015). Oligodendrocytes extend motile and exploratory processes that grow toward and connect with the appropriate axons (Kirby et al., 2006; Hughes et al., 2013). When oligodendrocyte-axon contacts are established, the thin cellular processes of oligodendrocytes transform into flat sheets that spread and wind along the axons to generate a multilayered stack of membranes that are tightly attached at their cytosolic and external surfaces. Myelin extends by two different concerted motions, the wrapping of the leading edge of the innermost layer of the growing myelin sheath around the axon, together with the lateral extension of all myelin membrane layers along the axon (Snaidero et al., 2014). Thus, for myelin growth, forces are required to continuously displace myelin from the axon by newly made layers of membrane from underneath and also to facilitate growth of the leading edge itself around and along the axon. In general, cells use the forces of F-actin polymerization at the cell front to push out membrane protrusions that subsequently become anchored to the extracellular substrate by transmembrane adhesion receptors (Ridley, 2011). These receptors are dynamically coupled to the actin cytoskeleton to provide grip for the transduction of the internal forces that are generated by actomyosin contractility and actin polymerization (Mitchison and Kirschner, 1988; Hu et al., 2007). In contrast, non-adhesive cells, such as leukocytes, can apply actin-network contractility to generate hydrostatic pressure for the induction of bleb-based membrane protrusions (Lämmermann and Sixt, 2009; Paluch and Raz, 2013). For such adhesion-independent modes of locomotion confinement within a 3D environment is critical for force transmission (Lämmermann et al., 2008; Liu et al., 2015). Whereas we understand the basic principles of how a "growth cone" operates in an elongating axon (Suter and Forscher, 1998; Lowery and Van Vactor, 2009; Vitriol and Zheng, 2012), we know little about the molecular machinery that drives the leading edge of the innermost wrap of myelin, which exists in a highly confined environment at the interface with its associated axon. To address this question, we used an array of different techniques and an interdisciplinary approach including in vivo live-imaging in zebrafish, mouse genetics, and biophysical analyses in cell culture. Based on these experiments, we propose that the protrusive forces of F-actin are used to

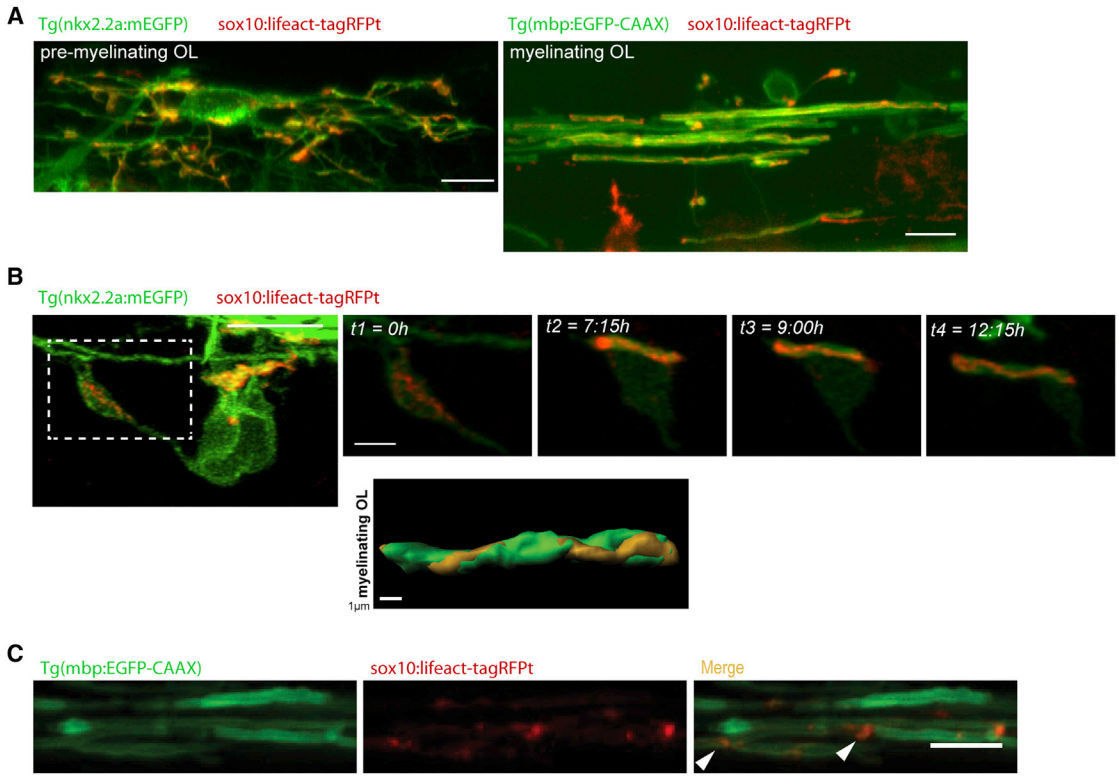

Figure 1. Localization and Dynamics of Filamentous Actin during Myelin Formation in Zebrafish

(A) Left, premyelinating oligodendrocyte visualized with membrane-targeted GFP using Tg(nkx2.2a:meGFP); right, myelinating oligodendrocyte visualized using Tg(mbp:EGFP-CAAX) zebrafish lines. The zebrafish were injected with a plasmid encoding for Lifeact, fused with the red fluorescent protein tag-RFPt under control of sox10 upstream regulatory sequences to localize F-actin. The scale bars represent 10 μm.

(B) Time-lapse imaging of Lifeact-RFP in Tg(nkx2.2a:meGFP) zebrafish at initial stages of myelination. The Lifeact-RFP moves in a spiral pattern longitudinally along the axon. The scale bars represent 10 μm (zoom in images, 3 μm).

(C) At later stages, using Tg(mbp:EGFP-CAAX) and Lifeact-RFP, F-actin is found at the lateral edges—presumably the paranodes—of the myelin sheaths (arrow heads). The scale bar represents 5 μm.

See also Movies S1 and S2.

push out a non-adhesive and motile leading edge, whereas subsequent F-actin disassembly induces its collapse and increases its adhesion to the substratum. We propose that iteration of such F-actin turnover drives the wrapping of myelin around axons.

RESULTS

Visualization of F-Actin Dynamics during Myelin Growth In Vivo

To visualize F-actin localization during myelin growth in vivo, we used zebrafish as a model organism, given its advantages for high-resolution in vivo imaging of myelin formation (Kirby et al., 2006; Czopka et al., 2013). To analyze the initial stages of CNS myelination, we utilized the Tg(nkx2.2a:meGFP) animal line, which expresses a membrane-tethered EGFP in a subset of oligodendrocyte precursor cells, pre-myelinating oligodendrocytes, and early myelinating oligodendrocytes (Kirby et al., 2006). F-actin distribution and dynamics were resolved by co-expressing Lifeact (here fused with the red fluorescent protein tag-RFPt under control of sox10 upstream regulatory sequences), which binds to F-actin and allows imaging for several hours without interfering with actin polymerization dynamics (Riedl et al., 2010).

We first imaged Lifeact-RFP in pre-myelinating oligodendrocytes and found that it broadly localized throughout the network of cellular processes and was often enriched at the tips of exploratory growth cone-like processes (Figure 1A). When cells were imaged at a later stage, we observed a very different distribution of F-actin (labeled by Tg(mbp:GFP-CAAX)), where F-actin was localized in a thin spiral along individual myelin sheaths (Figure 1A and Movie S1). Strikingly, just prior to axonal contact, F-actin was restricted to the outermost rim of the expanding and flattening oligodendroglial process (Figure 1B and Movies S2 and S3). When myelination started, F-actin moved in a spiral pattern longitudinally along the axon (Figure 1B and Movie S2). During myelination, Lifeact-RFP and membrane-tethered EGFP remained in distinct patterns, with F-actin forming a spiral and labeling a smaller fraction of the growing myelin sheath as compared to membrane-tethered EGFP (~28 ± 7% of Lifeact-RFP overlapping with membrane-tethered EGFP area, from ten different animals) (Figure 1B). We visualized myelin sheath maturation at later stages and found that Lifeact-RFP started to accumulate at the lateral edges—presumably the

paranodes—of the myelin sheaths (Figure 1C). Together, these results suggest that F-actin localizes to the leading edge and moves laterally with the expanding myelin sheath. Later, when longitudinal growth is completed, F-actin becomes restricted to the paranodal region of the myelin sheath. Thus, filamentous actin distribution within oligodendrocytes changes dramatically upon initiation of myelin sheath growth, when it localizes to the putative leading edge, where we have previously shown myelin growth to occur (Snaidero et al., 2014).

Adhesion-Independent Mode of Leading Edge Protrusion in Oligodendrocytes

At the onset of mouse spinal cord myelination (postnatal day [P] 4), F-actin is confined to the internal regions of the growing myelin sheath (Snaidero et al., 2014), but disappears almost completely from myelin at P13, when myelin growth is coming to an end (Figure S1A). The localization of F-actin to the leading edge region at the time of myelin growth further points to a role of actin in myelin wrapping. The F-actin-rich leading edge at the inner tongue is difficult to specifically visualize in the growing myelin sheath in vivo; therefore, for mechanistic analyses, we turned to primary cultures of oligodendrocytes that form flat sheets with a molecular composition similar to compacted myelin in vivo as a model system (Dubois-Dalcq et al., 1986; Aggarwal et al., 2011). By immunofluorescent analyses, we found that immature oligodendrocytes that just start to form membrane sheets generate numerous F-actin-rich lamellipodia-like protrusions along their processes. This is followed by the generation of membrane sheets that contain myelin basic protein (MBP), but only minor amounts of F-actin (Figure S1) (Dubois-Dalcq et al., 1986; Wilson and Brophy, 1989; Dyer and Benjamins, 1989; Song et al., 2001; Aggarwal et al., 2011). Strikingly, F-actin is almost completely depleted from differentiated oligodendrocytes, when it becomes confined to the outer rim, a structure reminiscent in appearance of a lamellipodium in migrating cells and analogous to the leading edge of the myelin sheath in vivo (Figure S1B).

The lamellipodium is usually where adhesion is initiated. Since adhesive strength is a key factor in controlling the mode of cellular locomotion (Ridley, 2011), we used interference reflection microscopy (IRM) to visualize cell adhesion and membrane dynamics during oligodendrocyte and myelin sheet growth in time-lapse experiments. This method relies on the destructive interference present in light reflected from the coverglass-liquid and liquid-lower cell membrane interfaces, which allows for the label-free estimation of inter-surface distances between a cell and a flat substratum. The resulting dark zones in the IRM images correspond to close contact, whereas non-adhesive areas appear bright. At early stages, when oligodendrocyte precursor cells grown on poly-L-lysine coated coverslips start to extend processes, a growth-cone like structure situated at the tip of each process showed mostly destructive interference in IRM images, suggesting tight apposition, and by inference close adhesion, between membrane and substrate (Figure 2A). Similar to neuronal growth cones, these structures contained multiple adhesion sites that were visualized by immunostainings with antibodies against vinculin (Figure 2C). As expected, when cultures were treated with trypsin (200 μg/ml), the growth cones retracted rapidly (within 15 min), demonstrating that adhesive contacts are required for its assembly (Figure 2B and Movie S3).

Surprisingly, when oligodendrocytes were imaged at a time when the cells were starting to generate membrane sheets, a "leading edge" with relatively large amounts of motile, non-adhesive membrane was found along the cellular processes (Figure 2A and Movie S4). After sheets had formed, the motile leading edge became restricted to the outer cellular rim. By introducing Lifeact-GFP into the cells, we observed that these motile, non-adhesive areas were enriched in F-actin (Movie S4). When trypsin (200 μg/ml) was added and adhesion and membrane dynamics imaged by IRM, we observed that the leading edge was unaffected by trypsin treatment, suggesting that focal adhesive contacts are not essential for its function (Figure 2B and Movie S5). In addition, vinculin was almost undetectable in the leading edge of cells plated either on poly-L-lysine or fibronectin (Figures 2C and 2D). To provide a comparison, we immunostained astrocytes for vinculin and found much higher levels (Figures 2C and 2D).

We performed time-lapse imaging of oligodendrocytes to visualize the development of the leading edge. We found that the leading edge extended in between the cellular processes to generate myelin membrane sheets (Movie S6). When cells were imaged at a time when myelin membrane sheet growth was completed, the leading edge was almost undetectable and mostly areas with tight apposition between membrane and the substrate were detected in the IRM movies (Movie S7).

Thus, when oligodendrocytes have fully extended their thin processes, the growth cones situated at the tip of each process disappears; instead the cells start to form large amounts of non-adhesive protrusions along their processes that extend and generate membrane sheets. A graphical scheme illustrating the localization of the leading edge during oligodendrocyte differentiation is shown in Figure S1.

F-Actin Depolymerization Triggers Adhesion and Membrane Spreading

The leading edge of most moving or growing cells anchors on to a substrate to generate a frictional interface. Without friction the cytoskeleton slips backward and the leading edge remains stationary. In contrast, non-adhesive cells, such as leukocytes, can generate friction by clamping the leading front between two surfaces with a 3D environment (Renkawitz and Sixt, 2010). We speculated that oligodendrocytes, similar as some leukocytes, use F-actin polymerization to "inflate" the leading edge into a 3D environment when they are generating myelin, instead of spreading it onto a 2D surface. If oligodendrocytes, indeed, push out membrane protrusions into 3D space during myelin formation, we hypothesized that by experimentally inducing F-actin depolymerization, we should be able to trigger the collapse and spreading of these protrusions onto the 2D substratum.

To test this idea, we treated cells that had extended their thin processes with latrunculin A to depolymerize F-actin and used combined confocal IRM and fluorescence microscopy to visualize the response. Indeed, within minutes after latrunculin A was added, membrane motility ceased and adhesive contacts were triggered (Figures 2E, 2F, and S2). Lifeact-GFP was excluded from these newly forming adhesive areas (Movie S8). Non-transfected cells showed similar results (Movie S8). We

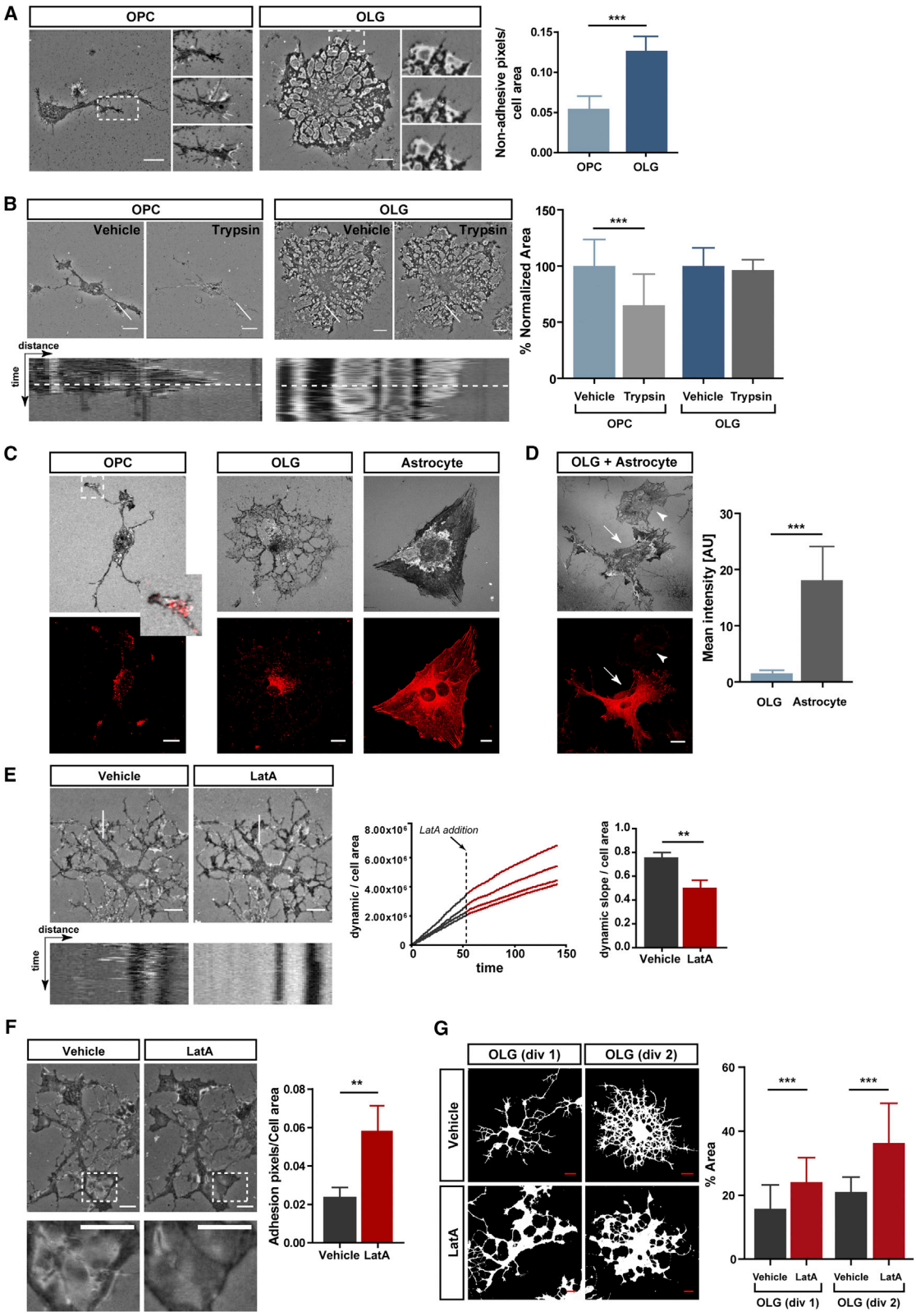

Figure 2. F-Actin Depolymerization Triggers Cell Adhesion and Membrane Spreading

(A) Live imaging of cell adhesion using IRM to visualize membrane dynamics and to measure the inter-surface distances between oligodendrocytes and the substratum. The resulting dark zones in IRM images correspond to close contact, whereas non-adhesive areas appear bright. The images show an

(legend continued on next page)

quantified the extent of membrane spreading and observed a striking increase in cell surface projection area after treating cells with latrunculin A (Figure 2G). Such a response to F-actin depolymerization is unusual, as one important function of F-actin is to increase the adhesiveness through linkages to adhesion molecules and supports our view of an adhesion-independent and deformation-based mode of leading edge protrusion. In contrast, when cells were treated with jasplakinolide, an actin stabilizing probe, we observed a reduction of cell motility and a slight decrease of cell surface projection area and adhesion (Figure S2).

An alternative explanation of our results is that actin depolymerization triggers exocytosis or/and blocks endocytosis, thereby increasing plasma membrane surface area (Diz-Muñoz et al., 2013). We used whole-cell patch-clamp to measure changes in cell surface area after actin depolymerization, but we did not detect any alterations suggesting that membrane is recruited from the flattening out of cell surface protrusions or folds (Figure S2).

Overall, our data indicate that oligodendrocytes generate membrane protrusions at the cell surface, which spread onto the substratum through F-actin depolymerization, during myelin growth. Since membrane spreading occurs without changes in the total surface area, the process implies that intracellular volume must have decreased and compaction occurred.

F-Actin Depolymerization Reduces Surface Tension

How does actin depolymerization trigger cell surface spreading in myelin forming oligodendrocytes? To understand how cell spreading is induced, it is instructive to compare cell spreading with liquid wetting: viscous liquid drops spread onto a surface, if the net loss in free energy through adhesion is larger than the "work" against surface tension (Sackmann and Bruinsma, 2002; Lecuit and Lenne, 2007). Thus, we hypothesized that F-actin disassembly triggers cell spreading and membrane adhesion by reducing membrane tension and thereby reducing the force against area dilatation. To measure membrane tension, we used an optical trap setup, which allowed us to determine membrane tension in flat cells by pulling small membrane tubes ("tethers") in the vertical direction, away from the surface of the adhered cell (Bodensiek et al., 2013). The force necessary to generate these tethers is largely determined by the interaction of the membrane with the actin cortex and the membrane bending rigidity (Sheetz and Dai, 1996). These experiments revealed a static tether force of ~11 pN (a value slightly lower to that of fibroblasts ~13 pN, *$p < 0.05$, and t test) in immature oligodendrocytes (branched, but without sheets) (Figure 3A). When similar experiments were performed with mature oligodendrocytes (with sheets), much lower static tether forces (~6 pN) were measured (Figure 3A). This shows that membrane tension declines with the onset of myelin sheet growth. Strikingly, when latrunculin A or cytochalasin D were applied to depolymerize the F-actin network in immature oligodendrocytes (with branches, but without sheets), the measured force dropped to values of mature cells (tether force of ~6 pN) (Figure 3A). In contrast, treatment with blebbistatin or Y27631, inhibitors of actomyosin contractility, did not affect membrane tension (Figure 3A). Thus, our results show that myelin membrane sheet formation is accompanied by a reduction in membrane tension, which is mainly attributed to the loss of F-actin.

Our model implies that oligodendrocytes build up tension at the leading edge by actin polymerization. Thus, we speculated that surface tension is non-homogenous and would be higher at the leading edge of the cell. We used atomic force microscopy (AFM) to map surface tension by pulling membrane tethers with the cantilever at different positions of the cell (Figure S3). As in our laser trapping experiments, we confirmed with AFM that membrane tension was F-actin dependent and higher in immature cells as compared to mature cells (Figures 3B and 3C). Since the tether forces as measured by AFM are obtained while pulling on the tether, the reported values are systematically higher than the static tether forces that were obtained by the optical trap at rest (Heinrich et al., 2005). Furthermore, and according to our predictions, significantly higher values were found at the outer cellular rim, the actin-rich leading edge, as compared to areas near the cell body or the sheets (Figure 3C). Overall, our data indicate that oligodendrocytes generate surface tension at the leading edge by F-actin polymerization. Depolymerization of F-actin reduces tension and induces membrane spreading and membrane sheet growth.

oligodendrocyte precursor (OPC) that is starting to extend processes and an oligodendrocyte (OLG) that has already formed processes, but is starting to generate membrane sheets. The inset is an enlarged area of the leading edge of the cells at different time points. The quantification shows an increase of non-adhesive membrane when comparing OPCs with OLGs. The bars represent mean ± SD (n = 9–15 cells from each stage, ***$p < 0.001$, and t test). The scale bar represents 10 μm.

(B) IRM images of OPCs and OLGs 15 min before and after incubation with 200 μg/ml trypsin. The kymographs are from the area indicated by white lines in the upper panel. The lower panel is a kymograph showing movement 15 min before and after treatment, the dotted line marks the point when trypsin was added. The quantification of changes in surface area of cells treated for 10 min with trypsin are shown. The cell surface area was quantified as described in (G) and normalized to untreated cells. The bars represent mean ± SD (n = 25–38 cells, ***$p < 0.001$, and t test). The scale bar represents 10 μm.

(C) Vinculin staining (red) of OPCs (left) and OLGs (middle) grown on poly-L-lysine coated coverslips. The inset shows an enlarged area of the growth-like structure of the OPC. An astrocyte (right) is shown as a comparison. The scale bar represents 10 μm.

(D) Vinculin staining (red) of an oligodendrocyte (arrow head) and an astrocyte (arrow) cultured for 4 days on 100 μg/ml poly-L-lysine + 100 μg/ml fibronectin coated coverslips. The quantification of mean fluorescent intensity between OLGs and astrocytes is shown. The bars represent mean ± SD (n = 14 cells each, ***$p < 0.001$, and t test). The scale bar represents 10 μm.

(E and F) (E) IRM was used to quantify changes in cell adhesion in OLGs treated with 10 μM latrunculin A (LatA). The quantification shows a decrease in membrane motility and an increase in adhesion area (F) within 30 min of incubation with LatA. The bars show mean ± SEM (n = 9 cells, **$p < 0.01$, and paired t test). The scale bar represents 10 μm.

(G) OLGs cultured for 1–2 days were treated with 10 μM LatA, incubated for 4 hr, and labeled with cell mask orange to visualize the cell surface. The cells are depicted as a binary image. A circle was fitted around the cell, and the cell surface area within the circle was determined and is given in percent. The bars show mean ± SD (n = 18–32 measurements, **$p < 0.01$, ***$p < 0.001$, and t test). The scale bar represents 10 μm.

See also Figures S1 and S2 and Movies S3, S4, S5, S6, S7, and S8.

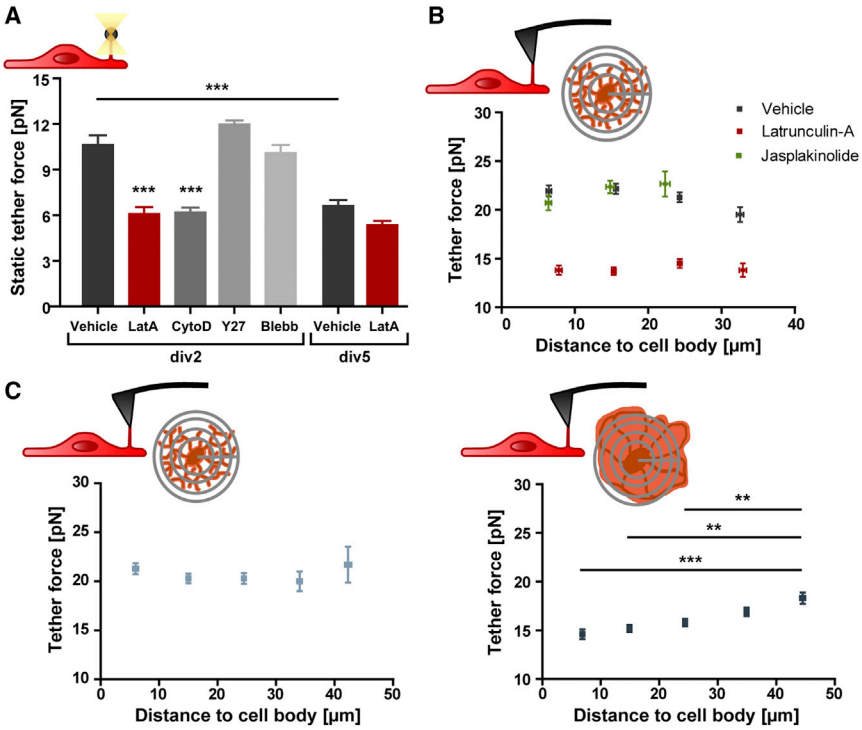

Figure 3. F-Actin Depolymerization Reduces Membrane Tension

(A) To measure surface tension in oligodendrocytes, we used an optical trap setup to pull membrane tubes (tethers) in a vertical direction with high force resolution. We cultured cells for 2 and 5 days in vitro (div). Treatment for 2 hr with 5 μM LatA and 5 μM cytochalasin D (CytoD) reduced tether forces, whereas 50 μM blebbistatin (Blebb) and 10 μM Y27631 (Y27) had no effect. The static tether force is shown as mean ± SEM (n = 37–80 cells for each condition and ***p < 0.001).

(B) AFM was used to measure membrane tension at different positions of the cell. The measured tether force is shown in relation to the distance from the cell body. The force map shows oligodendrocytes cultured for 2 days and treated with LatA, jasplakinolide, or vehicle, respectively. The tether force is shown as mean ± SEM (n = 10–13 cells, with a total of 67–245 pulled tethers per treatment).

(C) AFM was used to generate force maps of oligodendrocytes cultured for 2 days (left) and five days (right). The tether force was anisotropic in sheath forming cells with higher values in the outer cellular rim (**p < 0.01, ***p < 0.001, one-way ANOVA, and Tukey's multiple comparison test). The tether force is shown as mean ± SEM (n = 9–12 cells, with a total of 291–800 pulled tethers for each stage). See also Figure S3.

The Actin Depolymerizing Factors ADF and Cofilin1 Establish Low F-Actin/G-Actin Ratios

We propose that there are two iterative phases in the extension of the leading edge, the first, a polymerization driven protrusion phase, and the second, a depolymerization driven spreading phase. If so, high F-actin turnover rates are necessary. Low local F-actin/G-actin (F/G)-actin ratios are one indication of elevated filament assembly rates (Lee et al., 2013).

Thus, we determined the levels of monomeric actin (G) and polymeric (F) actin by biochemical and immunofluorescence-based assays in oligodendrocytes. Both approaches revealed a relative increase in the amount of G-actin at the expense of F-actin with cellular differentiation (Figures 4A and 4B). When G- and F-actin levels were determined in brain sections of the corpus callosum, a similar shift from polymeric toward monomeric actin was detected at the onset of myelination (Figure 4C). As these results suggested high F-actin disassembly rates, we set out to identify the responsible regulators. A transcriptome database (Cahoy et al., 2008) search revealed that several gene products involved in F-actin turnover are enriched in oligodendrocytes, of which gelsolin and proteins of the ADF/Cofilin family were prime candidates of such an activity (Bernstein and Bamburg, 2010). Since gelsolin knockout mice were viable with no obvious neurological deficits and no major alterations of myelin structure (data not shown), we turned to proteins of the ADF/Cofilin family. Western blotting of cell lysates prepared from oligodendrocytes at different time points of differentiation showed that these proteins were indeed upregulated at the time of myelin sheet biogenesis (Figure S4). To analyze their role in myelin biogenesis, we used mutant mice in which ADF and oligodendroglial-targeted cofilin1 were specifically deleted. As both proteins have significant functional redundancy and single deletions were without neurological deficits (data not shown), we generated ADF and cofilin1 double knockouts (DKO) by crossing *ADF* KO ($ADF^{-/-}$) with oligodendroglial-targeted *cofilin1* KO mice ($Cnp1\text{-}Cre^{+/-}{*}Cofilin^{flox/flox}$) (Figure S5).

We analyzed the amount of polymeric (F) and monomeric actin (G) in primary oligodendrocytes from DKO mice and observed a striking increase of F-actin levels at the leading edge when comparing to cells from control mice, both at early and late stages of differentiation (Figures 5A and 5B). In addition, cell surface area was reduced in oligodendrocytes cultured from DKO and partially rescued when inducing F-actin depolymerization by latrunculin A (Figure 5A).

Next, we analyzed the F-actin distribution in spinal cord cross-sections at P12, a time when the most active growth phase of myelin has passed. Whereas F-actin was almost undetectable in control animals, there was a dramatic increase of F-actin levels in the myelin sheath of *ADF/cofilin1* DKO mice (Figure 5C). When F/G-actin ratios were determined in spinal cord white matter, significantly higher ratios were observed in *ADF/cofilin1* DKO mice as compared to the control (Figure 5D). Thus, the activity of ADF/cofilin1 is responsible for generating low F/G-actin ratios in oligodendrocytes. Since our model of myelin growth predicts that high F-actin turnover rates are necessary, we hypothesized that *ADF/cofilin1* KO should generate thinner myelin sheaths.

ADF/Cofilin1 Are Involved in Myelin Growth

ADF/cofilin1 DKO animals were born at the expected Mendelian ratio, but developed severe motor deficits approximately 2 weeks after birth. The phenotype increased in intensity in the following days, resulting in animals with hind-limb paralysis, ataxia, and tremor that had to be sacrificed at ~P17.

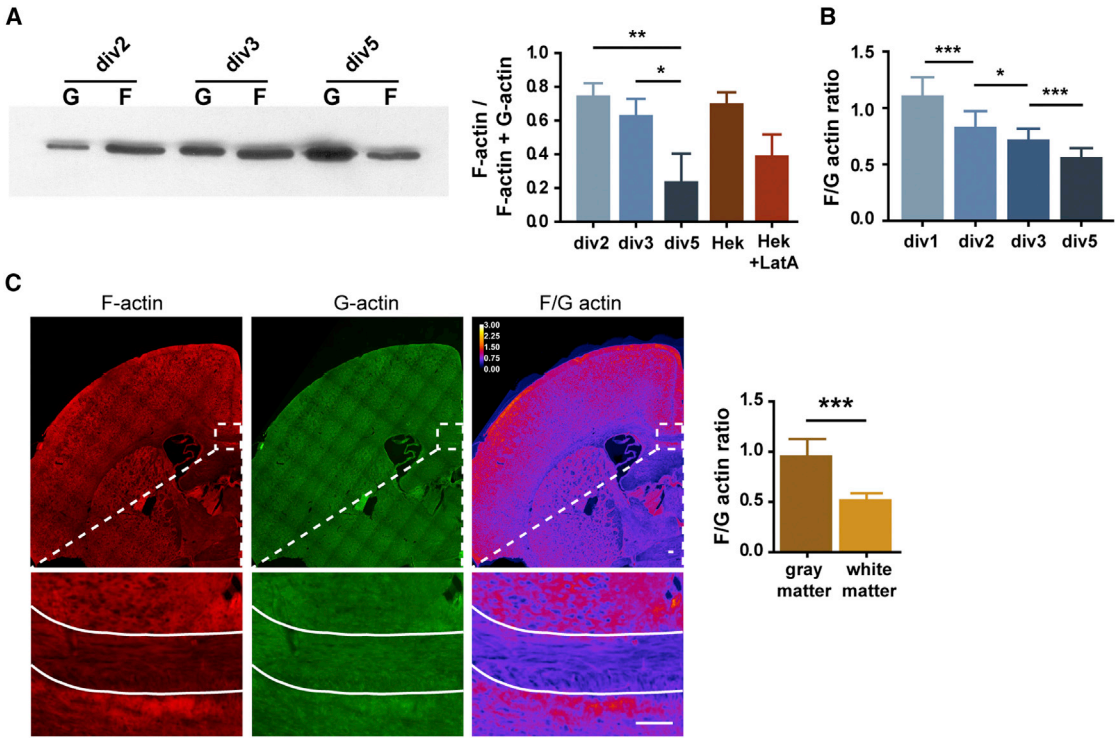

Figure 4. Low Ratios of Polymeric versus Monomeric Actin in Oligodendrocytes

(A) F- to G-actin ratios were quantified in cultured oligodendrocytes after 2, 3, and 5 days in vitro (div). The insoluble F-actin pool was separated from the soluble G-actin pool using Triton X-100 extraction and subsequent centrifugation. The fractions were immunoblotted against actin. The HEK293 cells treated with LatA served as a control. The bars show mean ± SD (n = 3 experiments, *p < 0.05, **p < 0.01, and t test).

(B) Quantification of F- to G-actin fluorescence intensity ratios by staining oligodendrocytes from day 1 to day 5 in vitro with DNase I to visualize G- and phalloidin-rhodamine to label F-actin (n = 20 cells from three experiments, *p < 0.05, ***p < 0.001, and t test) is shown.

(C) Sections of P17 mouse brains were stained as above to visualize G- and F-actin levels. Shown is the ratio of F- to G-actin ratio imaging in pseudocolors to indicate the high intensity pixels. The quantification of F- to G-actin fluorescence intensity ratios in the corpus callosum (indicated by white line; white matter) and the region above the corpus callosum (above the white line; gray matter) (n > 20 images from different animals, bars show mean ± SD, ***p < 0.001, and t test) is shown. The scale bars represent 10 μm.

Since the spinal cord is among the first areas to be myelinated in the CNS, we used electron microscopy to compare the extent of myelination at P7, P13, and P17 in spinal cords of control and ADF/cofilin1 DKO mice. We saw profound effects on myelination. Although myelination started relatively normally at P7 (Figure 6A), clear differences in myelin ultrastructure were observed at P13 and at P17 (Figures 6A–6E). Whereas the fiber tracts of the dorsal column were almost entirely myelinated and myelin had acquired its full thickness in control mice, this was not the case for *ADF/cofilin1* DKO mice (Figure 6C). Electron microscopy (EM) analyses revealed that myelin sheath growth appeared to stall in *ADF/cofilin1* mutants after P7 (as assessed by g-ratio analyses of myelin thickness over time) (Figure 6B). In addition, inspection of the fine structure revealed major abnormalities with an increase of the leading edge/inner tongue size in *ADF/cofilin1* DKO mice (Figure 6D). This suggests that actin depolymerization is required to regulate the size of the inner tongue. Because the increase of the inner tongue size in *ADF/cofilin1* DKO mice might confound our g-ratio analysis, we also measured the diameter of the compacted membrane stacks and found a clear reduction in myelin thickness, according to this measure in *ADF/cofilin1* DKOs as compared to the control (Figure 6E). In addition, although control animals show a dramatic increase in myelinated axon number from P7–P17, we observed only a modest increase in the number of myelinated axons in *ADF/cofilin1* DKO from P7–P17 (Figure 6E), implicating actin depolymerization as a major factor in regulating myelin sheath growth. To analyze possible effects on oligodendrocyte differentiation of *ADF/cofilin1* DKO, we determined the number of oligodendrocytes precursor and mature oligodendrocytes. No major differences were observed, indicating that the phenotype observed in *ADF/cofilin1* DKO cannot be explained by cell loss and is specific to myelination (Figure S6).

We also asked whether *ADF/cofilin1* is required to maintain myelin after developmental myelination is completed. To test this, we created tamoxifen-inducible conditional DKO mice by crossing ADF$^{-/-}$ with *cofilin1*$^{flox/flox}$*Plp1-CreERT2*. When the DKO was induced at P21, when myelination is completed in the spinal cord, and animals were analyzed 9 weeks later, no major differences in the number of myelinated axons and myelin thickness (g-ratio) were detected.

Overall, these data show that ADF/cofilin1 are major regulators of actin filament disassembly in oligodendrocytes, an activity that is important for myelin growth.

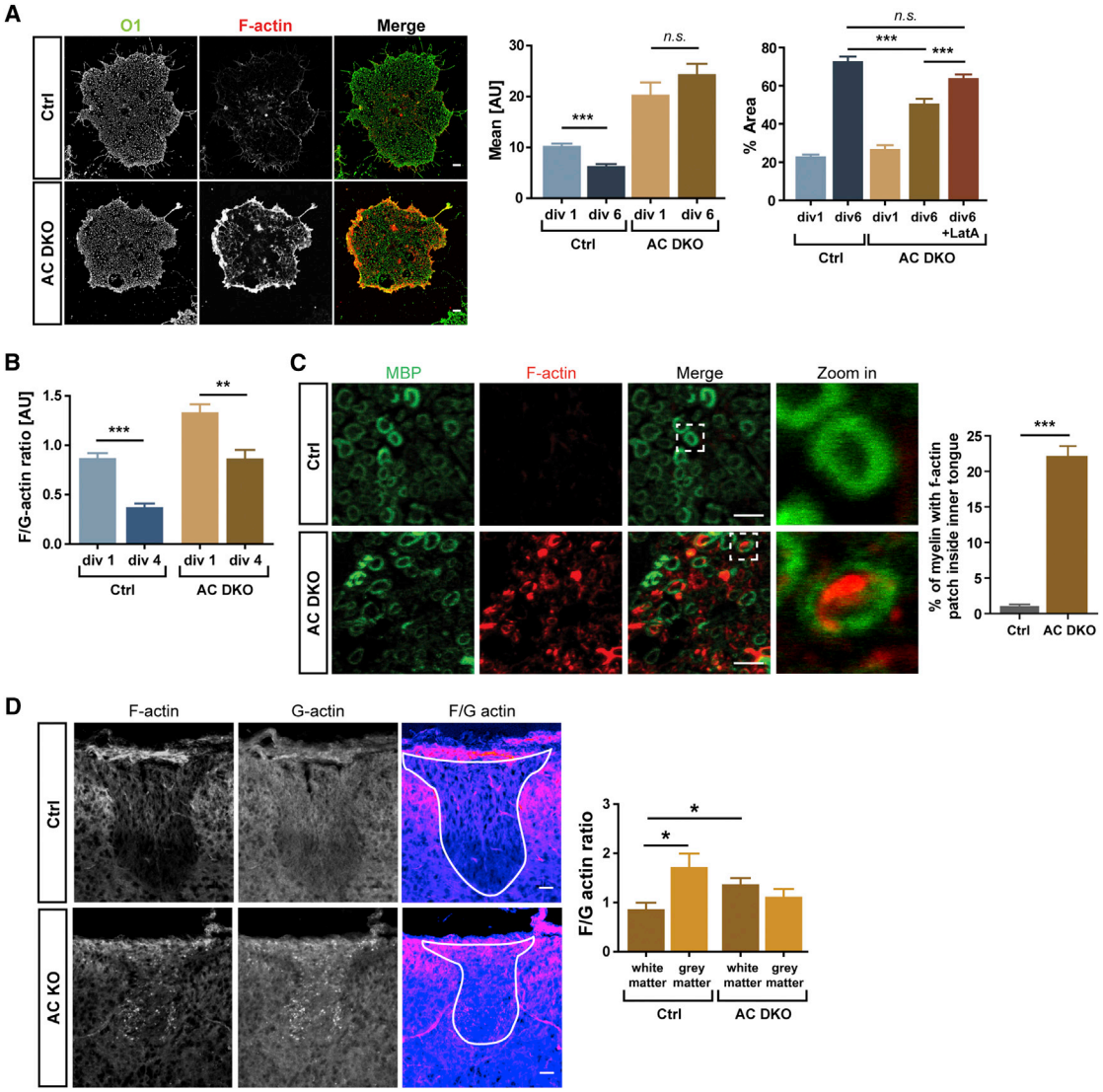

Figure 5. ADF/Cofilin1 Activity Is Required for F-Actin Disassembly in Oligodendrocyte

(A) Oligodendrocytes were cultured from *ADF/cofilin1* KO (AC DKO) and littermate control mice and stained for F-actin using rhodamine-phalloidin and with antibodies against galactosylceramide (O1) to visualize the cell surface (DIV6). The quantification of F-actin fluorescence intensity (mean AU) and cell surface projection area (n = 26–52 cells from three experiments, bars show mean ± SEM, $^{**}p < 0.01$, $^{***}p < 0.001$, and t test) is shown. The scale bars represent 10 μm.

(B) Oligodendrocytes were cultured from controls (ADF KO) and *ADF/cofilin1* KO (AC DKO) mice and F- to G-actin fluorescence intensity ratios were quantified from stainings with DNase I to visualize G- and phalloidin-rhodamine to label F-actin (n = 17–40 cells from three experiments, bars show mean ± SEM, $^{**}p < 0.01$, $^{***}p < 0.001$, and t test).

(C) Localization of F-actin and MBP in spinal cord sections (400 nm thick) of control and *ADF/cofilin1* DKO mice at P12. The percentage of myelinated axons showing F-actin labeling within sheaths using rhodamine-phalloidin are shown. The bars show mean ± SEM (n = 3, 874–1,266 myelinated axons per animal, $^{***}p < 0.001$, and t test). The scale bars represent 5 μm.

(D) Sections of P17 mouse spinal cords from control (ADF KO) and *ADF/cofilin1* DKO (AC DKO) mice were stained to visualize G- and F-actin levels. Also shown is the ratio of F- to G-actin ratio imaging in pseudocolors to indicate the high intensity pixels. The quantification of F- to G-actin fluorescence intensity ratios in the gray (area outside of the white line) and white matter (indicated by a white line) (n > 10 images from four animals, bars show mean ± SEM, $^{*}p < 0.01$, and t test) is shown. The scale bars represent 10 μm.

See also Figures S4 and S5.

DISCUSSION

Whereas the basic principles of axonal elongation have been solved, the mechanisms of myelin growth are poorly understood. The basic question such as the definition of the forces driving the leading edge multiple times around the axon has been difficult to address. The complexity arises from the localization of the leading edge within a multilayered membrane, where new layers of membrane are added from underneath. A striking feature in myelination is that two membrane surfaces—axonal and

glial—need to remain in close contact and to move one upon the other over long distances.

Which forces drive membrane wrapping? We observe that F-actin is almost entirely depleted from myelin sheaths, but most likely remains concentrated at the leading edge at the inner tongue during active growth. Since the leading edge of myelinating oligodendrocytes is localized in the interior of the myelin sheath and is, thus, not directly accessible for microscopic analysis, we used cultured oligodendrocytes as a model system to study its mechanisms. We find that the leading edge behaves differently from a lamellipodia of a neuronal growth cone.

Whereas a neuronal or an oligodendroglial precursor cell growth cone forms stable adhesions with the extracellular matrix for force transmission, the leading edge of oligodendrocytes appears to be relatively non-adhesive. Are focal adhesive contacts dispensable for myelin growth in vivo? When the leading edge of the growing myelin sheaths extends between the axon and inner layer of the myelin sheath, it interacts with membranes in all possible directions. This interaction may help to entangle the leading edge and to provide friction for the movement. Such a deformation-based mode of locomotion is reminiscent to leukocyte migration through a 3D environment in vivo, which is independent of adhesion-receptor mediated force transmission (Lämmermann et al., 2008). An alternative explanation is that the relevant axonal adhesion molecules necessary to clamp the leading edge of oligodendrocytes are missing in a culture dish. However, focal adhesion complexes are found in the growing front of most adherent cells in culture, but are absent from the leading edge of oligodendrocytes. In addition, oligodendrocytes are known to be able to wrap myelin around inert polystyrene fibers, supporting the idea of adhesion receptor-independent force generation (Lee et al., 2012).

Interestingly, a recent study shows that in the absence of focal adhesions and under conditions of confinement, cells that are usually not capable of amoeboid motility can switch from an adhesive mesenchymal to a non-adhesive amoeboid mode of migration (Liu et al., 2015). There were two modes of non-adhesive amoeboid motility that were identified, one involving high cell contractility with global cortical actin flow (Liu et al., 2015; Ruprecht et al., 2015) and another requiring low contractility, but relying instead on local actin polymerization (Liu et al., 2015). Thus, one distinguishing feature in cells using non-adhesive modes of force transmissions is the extent of cortical contractility. Membrane tension was low in oligodendrocytes, ruling out actomyosin-based contractility and bleb-formation as a driving force in myelin wrapping.

Instead, we propose that the formation of flat myelin membrane sheets can be understood in terms of a wetting transition; i.e., the spreading of drops of liquids on a substrate. Spreading of a liquid drop enclosed by a membrane (wetting of the surface) occurs if both the bending of the membrane and the work against surface tension is exceeded by the gain in free energy though adhesion. It is instructive to compare cellular adhesion to the surface with wrapping of beads. If bending is assumed to be negligible, which is true for thin cortices below 500 nm thickness, adhesion energy and membrane tension are related through Young-Dupre's equation. Smaller surface tension and lower bending stiffness thus facilitates adhesion. If F-actin is present, both tension of the membrane is increased as well as the bending modules of the cortex-membrane shell. Therefore, low F-actin content along with plasma membrane reservoirs favors, while high cortical tension prohibits, adhesion.

Taken together, we propose that the forces of F-actin polymerization are used to inflate and to clamp the leading edge of the inner tongue within its 3D environment. By F-actin driven inflation, the leading edge pushes in between the axon and the growing myelin sheath, whereas the successive disassembly of the actin filament network may promote the spreading and the stable adhesion of myelin onto the axon (Figure 7). We identified ADF/cofilin1 as key regulators in this process. However, it is important to note that deletion of ADF/cofilin1 did not completely prevent myelin growth. A possible reason is the compensation by other depolymerizing factors such as cofilin2 or gelsolin.

Our model that regulated F-actin turnover is crucial in myelin formation is supported by studies, in which the actin cytoskeleton regulator, the neuronal Wiskott-Aldrich syndrome protein (N-WASP), was deleted in Schwann cells (Jin et al., 2011; Novak et al., 2011). Schwann cells lacking N-WASP failed to generate normal lamellipodia and consequently were unable to form myelin. In addition, in mice, myelin formation is impaired when the WASP family verprolin homologous (WAVE) or the Cdc42 and Rac1 GTPase cytoskeletal regulators are deleted (Kim et al., 2006; Thurnherr et al., 2006; Benninger et al., 2007).

Future experiments will be required to elucidate the molecular components and the signaling pathways that link axonal factors (Furusho et al., 2012; Lundgaard et al., 2013; Mensch et al., 2015, Hines et al., 2015) and potential remyelination therapeutics (Fancy et al., 2011; Huang et al., 2011; Deshmukh et al., 2013; Mei et al., 2014) to leading edge activity. Since the activity of ADF/cofilin1 is regulated by phosphorylation, it will be interesting to find out whether these signaling pathways are connected to actin dynamics.

EXPERIMENTAL PROCEDURES

Zebrafish Experiments and Analysis

All animals were maintained and experiments performed according to the UK Home Office guidelines. The transgenic zebrafish lines Tg(nkx2.2a:mEGFP), Tg(Sox10:mRFP), and Tg(mbp:mEGFP) were used for visualization of the oligodendrocyte membrane (Czopka et al., 2013). The imaging is described in the Supplemental Information.

Mice

All animal experiments were performed according to the Lower Saxony State regulations for animal experimentation. Mutant mice were bred and maintained on a C57BL/6 background. *Cnp*-Cre mice (Lappe-Siefke et al., 2003), *ADF* KO, and *cofilin1*$^{fl/fl}$ mice have been described previously (Bellenchi et al., 2007; Flynn et al., 2012). To generate oligodendrocyte-specific ADF/cofilin1 knockout, *Cnp-Cre* mice were crossbred with *cofilin1*$^{fl/fl}$ and crossed with *ADF* KO to generate *ADF* KO* *cofilin1*$^{flox/flox}$* *Cnp1-Cre*$^{+/-}$.

EM and Quantification

Mice were anesthetized using Avertin and perfused using 4% paraformaldehyde, 2.5% glutaraldehyde in 0.1 M phosphate buffer. Tissue was dissected and contrasted with 2% osmium tetroxide (OsO_4) in 0.1 M phosphate buffer and embedded in epoxy resin (Serva Electrophoresis). Using an ultramicrotome (Leica, RM2155), ultrathin sections were cut with a diamond knife (Histo HI 4317; Diatome) and contrasted. Electron microscopic images were taken using LEO EM912 transmission electron microscope and a 208 × 2,048 CCD camera (Proscan). To measure the g-ratio, the circumference of the outer layer of myelin, the layer surrounding the inner tongue, and the axon were

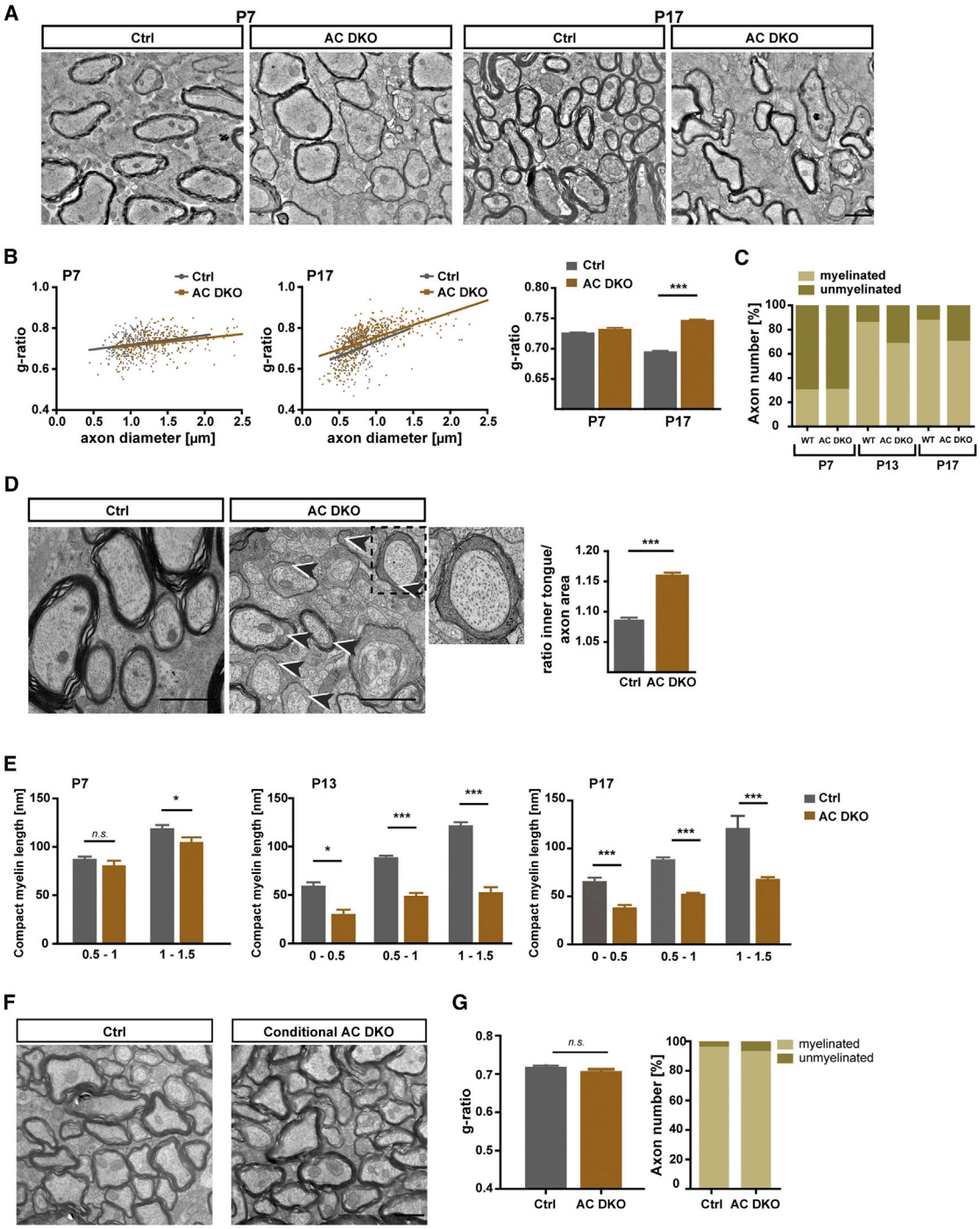

Figure 6. ADF/Cofilin1 Is Required for Myelin Growth in Mice

(A) Electron micrograph of cervical spinal cord of controls (*ADF*$^{+/+}$*cofilin*$^{flox/wt}$ *Cnp1-Cre*/+) and *ADF/cofilin1 DKO* (*ADF*$^{-/-}$*cofilin1*$^{flox/flox}$ *Cnp1-Cre*/+) mice at P7 and P17. The scale bar represents 1 µm.

(B) Scatter plots of g-ratios of individual fibers in relation to respective axon diameters quantified from *ADF/cofilin1 KO* (AC DKO; brown circles) and littermate controls (Ctrl; dark circles) at P7 and P17. The average g-ratio values (right) show that myelin thickness continues to increase in the Ctrls, but not in the *ADF/cofilin1* DKO (~100 axons from three to four mice of each age and genotype were analyzed and ***$p < 0.001$).

(C) Percentage of myelinated and unmyelinated axons, counted at P7, P13, and P17, shows that mutants myelinate less axons from P13 onward as compared to the Ctrl (~1,000 axons from >50 EM images of three to four mice were counted for each time point).

(D) Left, *ADF/cofilin1* DKO mice show increased inner tongues (arrows and inset). The quantification shows the larger diameter of the inner tongue (in relation to axonal size) in *ADF/cofilin1* KO at P17, as compared to the Ctrl (right). A ratio of one corresponds to no inner tongue.

(legend continued on next page)

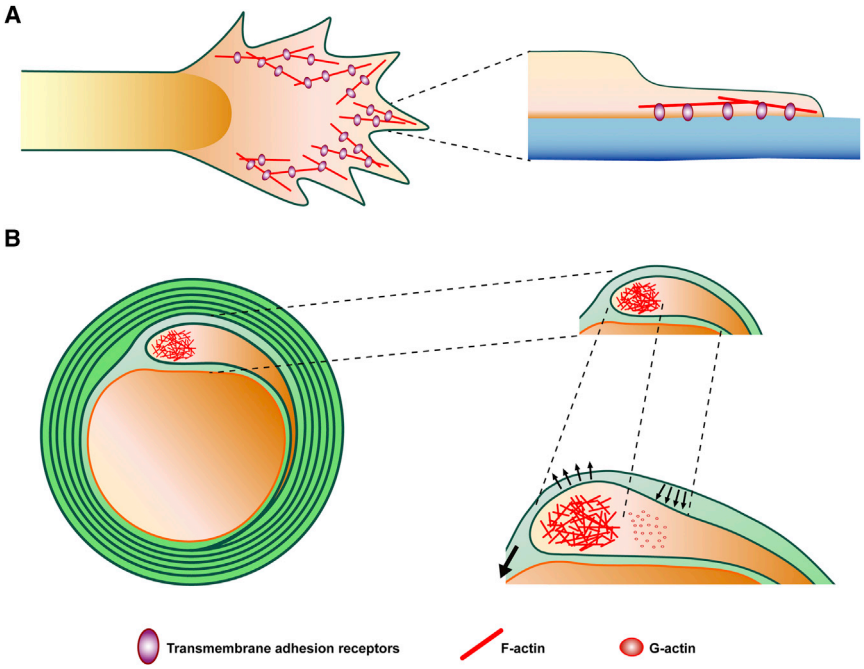

Figure 7. Model of the Role of F-Actin in Myelin Growth

(A) Cartoon showing the structure of a typical growth cone (e.g., in an elongating axon or an OPC). The growth cone is anchored to the extracellular substrate by transmembrane adhesion receptors (pink) to generate a frictional interface for force transmission.

(B) Cartoon showing the structure of the leading edge at the inner tongue of the myelin sheath. We propose that the polymerizing forces of F-actin push out membrane protrusions that squeeze in between the axon and the myelin sheath, whereas the subsequent disassembly of F-actin promotes adhesion and spreading. Thus, sustained cycles of actin-based in- and deflation (arrows) may drive extension and spreading of the growing myelin membrane.

measured using ImageJ. The diameter, length of compact myelin, or circumference was calculated using these data from each individual axon. A minimum of 300 myelinated cross-sections were measured per genotype and 100 per animal.

IRM and Quantification

For IRM, imaging cells were monitored using Leica SP5 confocal laser scanning microscope (CLSM) with a 63× objective (numerical aperture [NA] 1.3) or 40× (NA 1.25) and a laser illumination to minimize phototoxicity. The reflected light was collected using with a photomultiplier tube (PMT) detector every 14 or 34 s. The IRM time series were semi-automatically analyzed with a custom-written FIJI macro. Briefly, a "walking difference" routine was applied, which revealed pixels that reported dynamic changes in cell-surface adhesion. Pixel intensities above a threshold, which was kept constant for all experiments, were kept and applied toward the cell-surface adhesion quantification. Additionally, the cell footprint area was quantified after segmentation of the IRM signal with the Trainable Weka Segmentation plugin of FIJI. The cell-surface adhesion dynamics was normalized to the respective cell footprint area.

AFM Membrane Tension Measurements and Vertical Optical Trap Tether Extraction

A vertical optical trap has been described in Nawaz et al. (2012) and Bodensiek et al. (2013). The details of both procedures are described in the Supplemental Information.

Capacitance Measurements

Experimental procedures for whole-cell patch-clamp capacitance were as described previously (Hsu et al., 2010). The details are described in the Supplemental Information.

Statistical Analysis

Statistical significance was determined using GraphPad PRISM 5 software. Unless stated otherwise, the statistical analyses were performed using two-tailed Student's t test function (t test < 0.05: *; < 0.01: **; and < 0.001: ***). For comparing three or more groups, a one-way ANOVA was used and further pairwise using Tukey's post test.

SUPPLEMENTAL INFORMATION

Supplemental Information includes Supplemental Experimental Procedures, six figures, and eight movies and can be found with this article online at http://dx.doi.org/10.1016/j.devcel.2015.05.013.

AUTHOR CONTRIBUTIONS

Investigation: S.N., P.S., S.S., N.S., C.V., B.R.B., T.C., S.Y.J., J.S.R., A.J., I.A.T.S., and D.A.L. Resources: W.W. Visualization: S.N., P.S., and M.M. Software: I.A. and M.M. Conceptualization: S.N., P.S., and M.S. Supervision: M.S., D.A.L., and I.A.T.S. Writing of original draft: M.S. Writing, review, and editing: all authors.

ACKNOWLEDGMENTS

The work was supported by grants from the German Research Foundation (SI 746/9-1; SI 746/10-1 and 11-1; and SFB-TRR43), BMBF (E-rare), and the Tschira-Stiftung. The PLPCreERT2 mice have been used in collaboration with Ueli Suter. We thank Christine Gurniak for help with the KO mice. S.N., P.S., and I.A.T.S. were supported by the Cluster of Excellence and DFG Research Center Nanoscale Microscopy and Molecular Physiology of the Brain.

(E) Quantification of compacted myelin sheath thickness (in nm) in relation to respective axon diameter at P7, P13, and P17. Since very few axons with a diameter between 0–0.5 μm are myelinated at P7, the data for this time point are not shown. The bars show mean ± SEM (n > 100 axons per diameter range of three mice per genotype; *p < 0.05, ***p < 0.001, and t test).

(F) Electron micrographs of Ctrl (*ADF*$^{-/-}$**cofilin1*$^{fl/fl}$ **PLP-CreERT2*/− + Tamoxifen) and after conditional inactivation (*ADF*$^{-/-}$**cofilin1*$^{fl/fl}$ **PLP-CreERT2*/+ + Tamoxifen) are shown. The tamoxifen was injected at P21 and mice were analyzed 9 weeks later. The scale bar represents 2 μm.

(G) G-ratio analysis of Ctrl and conditional *ADF/cofilin1* KO mice are shown as mean ± SEM (~400 axons were quantified of at least three animals per genotype). The right shows the percent of myelinated axons, >300 axons were counted per animals, per genotype.

See also Figure S6.

Received: March 30, 2015
Revised: May 8, 2015
Accepted: May 18, 2015
Published: July 9, 2015

REFERENCES

Aggarwal, S., Yurlova, L., Snaidero, N., Reetz, C., Frey, S., Zimmermann, J., Pähler, G., Janshoff, A., Friedrichs, J., Müller, D.J., et al. (2011). A size barrier limits protein diffusion at the cell surface to generate lipid-rich myelin-membrane sheets. Dev. Cell *21*, 445–456.

Bauer, N.G., Richter-Landsberg, C., and Ffrench-Constant, C. (2009). Role of the oligodendroglial cytoskeleton in differentiation and myelination. Glia *57*, 1691–1705.

Bellenchi, G.C., Gurniak, C.B., Perlas, E., Middei, S., Ammassari-Teule, M., and Witke, W. (2007). N-cofilin is associated with neuronal migration disorders and cell cycle control in the cerebral cortex. Genes Dev. *21*, 2347–2357.

Benninger, Y., Thurnherr, T., Pereira, J.A., Krause, S., Wu, X., Chrostek-Grashoff, A., Herzog, D., Nave, K.A., Franklin, R.J., Meijer, D., et al. (2007). Essential and distinct roles for cdc42 and rac1 in the regulation of Schwann cell biology during peripheral nervous system development. J. Cell Biol. *177*, 1051–1061.

Bercury, K.K., and Macklin, W.B. (2015). Dynamics and mechanisms of CNS myelination. Dev. Cell *32*, 447–458.

Bernstein, B.W., and Bamburg, J.R. (2010). ADF/cofilin: a functional node in cell biology. Trends Cell Biol. *20*, 187–195.

Bodensiek, K., Li, W., Sánchez, P., Nawaz, S., and Schaap, I.A. (2013). A high-speed vertical optical trap for the mechanical testing of living cells at piconewton forces. Rev. Sci. Instrum. *84*, 113707.

Cahoy, J.D., Emery, B., Kaushal, A., Foo, L.C., Zamanian, J.L., Christopherson, K.S., Xing, Y., Lubischer, J.L., Krieg, P.A., Krupenko, S.A., et al. (2008). A transcriptome database for astrocytes, neurons, and oligodendrocytes: a new resource for understanding brain development and function. J. Neurosci. *28*, 264–278.

Czopka, T., Ffrench-Constant, C., and Lyons, D.A. (2013). Individual oligodendrocytes have only a few hours in which to generate new myelin sheaths in vivo. Dev. Cell *25*, 599–609.

Deshmukh, V.A., Tardif, V., Lyssiotis, C.A., Green, C.C., Kerman, B., Kim, H.J., Padmanabhan, K., Swoboda, J.G., Ahmad, I., Kondo, T., et al. (2013). A regenerative approach to the treatment of multiple sclerosis. Nature *502*, 327–332.

Diz-Muñoz, A., Fletcher, D.A., and Weiner, O.D. (2013). Use the force: membrane tension as an organizer of cell shape and motility. Trends Cell Biol. *23*, 47–53.

Dubois-Dalcq, M., Behar, T., Hudson, L., and Lazzarini, R.A. (1986). Emergence of three myelin proteins in oligodendrocytes cultured without neurons. J. Cell Biol. *102*, 384–392.

Dyer, C.A., and Benjamins, J.A. (1989). Organization of oligodendroglial membrane sheets: II. Galactocerebroside:antibody interactions signal changes in cytoskeleton and myelin basic protein. J. Neurosci. Res. *24*, 212–221.

Fancy, S.P., Harrington, E.P., Yuen, T.J., Silbereis, J.C., Zhao, C., Baranzini, S.E., Bruce, C.C., Otero, J.J., Huang, E.J., Nusse, R., et al. (2011). Axin2 as regulatory and therapeutic target in newborn brain injury and remyelination. Nat. Neurosci. *14*, 1009–1016.

Fields, R.D. (2008). White matter in learning, cognition and psychiatric disorders. Trends Neurosci. *31*, 361–370.

Flynn, K.C., Hellal, F., Neukirchen, D., Jacob, S., Tahirovic, S., Dupraz, S., Stern, S., Garvalov, B.K., Gurniak, C., Shaw, A.E., et al. (2012). ADF/cofilin-mediated actin retrograde flow directs neurite formation in the developing brain. Neuron *76*, 1091–1107.

Furusho, M., Dupree, J.L., Nave, K.A., and Bansal, R. (2012). Fibroblast growth factor receptor signaling in oligodendrocytes regulates myelin sheath thickness. J. Neurosci. *32*, 6631–6641.

Heinrich, V., Leung, A., and Evans, E. (2005). Nano- to microscale dynamics of P-selectin detachment from leukocyte interfaces. II. Tether flow terminated by P-selectin dissociation from PSGL-1. Biophys. J. *88*, 2299–2308.

Hines, J.H., Ravanelli, A.M., Schwindt, R., Scott, E.K., and Appel, B. (2015). Neuronal activity biases axon selection for myelination in vivo. Nat. Neurosci. *18*, 683–689.

Hsu, C., Morohashi, Y., Yoshimura, S., Manrique-Hoyos, N., Jung, S., Lauterbach, M.A., Bakhti, M., Grønborg, M., Möbius, W., Rhee, J., et al. (2010). Regulation of exosome secretion by Rab35 and its GTPase-activating proteins TBC1D10A-C. J. Cell Biol. *189*, 223–232.

Hu, K., Ji, L., Applegate, K.T., Danuser, G., and Waterman-Storer, C.M. (2007). Differential transmission of actin motion within focal adhesions. Science *315*, 111–115.

Huang, J.K., Jarjour, A.A., Nait Oumesmar, B., Kerninon, C., Williams, A., Krezel, W., Kagechika, H., Bauer, J., Zhao, C., Baron-Van Evercooren, A., et al. (2011). Retinoid X receptor gamma signaling accelerates CNS remyelination. Nat. Neurosci. *14*, 45–53.

Hughes, E.G., Kang, S.H., Fukaya, M., and Bergles, D.E. (2013). Oligodendrocyte progenitors balance growth with self-repulsion to achieve homeostasis in the adult brain. Nat. Neurosci. *16*, 668–676.

Jin, F., Dong, B., Georgiou, J., Jiang, Q., Zhang, J., Bharioke, A., Qiu, F., Lommel, S., Feltri, M.L., Wrabetz, L., et al. (2011). N-WASp is required for Schwann cell cytoskeletal dynamics, normal myelin gene expression and peripheral nerve myelination. Development *138*, 1329–1337.

Kim, H.J., DiBernardo, A.B., Sloane, J.A., Rasband, M.N., Solomon, D., Kosaras, B., Kwak, S.P., and Vartanian, T.K. (2006). WAVE1 is required for oligodendrocyte morphogenesis and normal CNS myelination. J. Neurosci. *26*, 5849–5859.

Kirby, B.B., Takada, N., Latimer, A.J., Shin, J., Carney, T.J., Kelsh, R.N., and Appel, B. (2006). In vivo time-lapse imaging shows dynamic oligodendrocyte progenitor behavior during zebrafish development. Nat. Neurosci. *9*, 1506–1511.

Lämmermann, T., and Sixt, M. (2009). Mechanical modes of 'amoeboid' cell migration. Curr. Opin. Cell Biol. *21*, 636–644.

Lämmermann, T., Bader, B.L., Monkley, S.J., Worbs, T., Wedlich-Söldner, R., Hirsch, K., Keller, M., Förster, R., Critchley, D.R., Fässler, R., and Sixt, M. (2008). Rapid leukocyte migration by integrin-independent flowing and squeezing. Nature *453*, 51–55.

Lappe-Siefke, C., Goebbels, S., Gravel, M., Nicksch, E., Lee, J., Braun, P.E., Griffiths, I.R., and Nave, K.A. (2003). Disruption of Cnp1 uncouples oligodendroglial functions in axonal support and myelination. Nat. Genet. *33*, 366–374.

Lecuit, T., and Lenne, P.F. (2007). Cell surface mechanics and the control of cell shape, tissue patterns and morphogenesis. Nat. Rev. Mol. Cell Biol. *8*, 633–644.

Lee, S., Leach, M.K., Redmond, S.A., Chong, S.Y., Mellon, S.H., Tuck, S.J., Feng, Z.Q., Corey, J.M., and Chan, J.R. (2012). A culture system to study oligodendrocyte myelination processes using engineered nanofibers. Nat. Methods *9*, 917–922.

Lee, C.W., Vitriol, E.A., Shim, S., Wise, A.L., Velayutham, R.P., and Zheng, J.Q. (2013). Dynamic localization of G-actin during membrane protrusion in neuronal motility. Curr. Biol. *23*, 1046–1056.

Liu, Y.J., Le Berre, M., Lautenschlaeger, F., Maiuri, P., Callan-Jones, A., Heuzé, M., Takaki, T., Voituriez, R., and Piel, M. (2015). Confinement and low adhesion induce fast amoeboid migration of slow mesenchymal cells. Cell *160*, 659–672.

Lowery, L.A., and Van Vactor, D. (2009). The trip of the tip: understanding the growth cone machinery. Nat. Rev. Mol. Cell Biol. *10*, 332–343.

Lundgaard, I., Luzhynskaya, A., Stockley, J.H., Wang, Z., Evans, K.A., Swire, M., Volbracht, K., Gautier, H.O., Franklin, R.J., Ffrench-Constant, C., Attwell, D., and Káradóttir, R.T. (2013). Neuregulin and BDNF induce a switch to NMDA receptor-dependent myelination by oligodendrocytes. PLoS Biol. *11*, e1001743.

Mei, F., Fancy, S.P., Shen, Y.A., Niu, J., Zhao, C., Presley, B., Miao, E., Lee, S., Mayoral, S.R., Redmond, S.A., et al. (2014). Micropillar arrays as a

high-throughput screening platform for therapeutics in multiple sclerosis. Nat. Med. *20*, 954–960.

Mensch, S., Baraban, M., Almeida, R., Czopka, T., Ausborn, J., El Manira, A., and Lyons, D.A. (2015). Synaptic vesicle release regulates myelin sheath number of individual oligodendrocytes in vivo. Nat. Neurosci. *18*, 628–630.

Mitchison, T., and Kirschner, M. (1988). Cytoskeletal dynamics and nerve growth. Neuron *1*, 761–772.

Nawaz, S., Sánchez, P., Bodensiek, K., Li, S., Simons, M., and Schaap, I.A. (2012). Cell visco-elasticity measured with AFM and optical trapping at sub-micrometer deformations. PLoS ONE *7*, e45297.

Novak, N., Bar, V., Sabanay, H., Frechter, S., Jaegle, M., Snapper, S.B., Meijer, D., and Peles, E. (2011). N-WASP is required for membrane wrapping and myelination by Schwann cells. J. Cell Biol. *192*, 243–250.

Paluch, E.K., and Raz, E. (2013). The role and regulation of blebs in cell migration. Curr. Opin. Cell Biol. *25*, 582–590.

Renkawitz, J., and Sixt, M. (2010). Mechanisms of force generation and force transmission during interstitial leukocyte migration. EMBO Rep. *11*, 744–750.

Ridley, A.J. (2011). Life at the leading edge. Cell *145*, 1012–1022.

Riedl, J., Flynn, K.C., Raducanu, A., Gärtner, F., Beck, G., Bösl, M., Bradke, F., Massberg, S., Aszodi, A., Sixt, M., and Wedlich-Söldner, R. (2010). Lifeact mice for studying F-actin dynamics. Nat. Methods *7*, 168–169.

Ruprecht, V., Wieser, S., Callan-Jones, A., Smutny, M., Morita, H., Sako, K., Barone, V., Ritsch-Marte, M., Sixt, M., Voituriez, R., and Heisenberg, C.P. (2015). Cortical contractility triggers a stochastic switch to fast amoeboid cell motility. Cell *160*, 673–685.

Sackmann, E., and Bruinsma, R.F. (2002). Cell adhesion as wetting transition? ChemPhysChem *3*, 262–269.

Sheetz, M.P., and Dai, J. (1996). Modulation of membrane dynamics and cell motility by membrane tension. Trends Cell Biol. *6*, 85–89.

Sherman, D.L., and Brophy, P.J. (2005). Mechanisms of axon ensheathment and myelin growth. Nat. Rev. Neurosci. *6*, 683–690.

Simons, M., and Lyons, D.A. (2013). Axonal selection and myelin sheath generation in the central nervous system. Curr. Opin. Cell Biol. *25*, 512–519.

Snaidero, N., Möbius, W., Czopka, T., Hekking, L.H., Mathisen, C., Verkleij, D., Goebbels, S., Edgar, J., Merkler, D., Lyons, D.A., et al. (2014). Myelin membrane wrapping of CNS axons by PI(3,4,5)P3-dependent polarized growth at the inner tongue. Cell *156*, 277–290.

Song, J., Goetz, B.D., Baas, P.W., and Duncan, I.D. (2001). Cytoskeletal reorganization during the formation of oligodendrocyte processes and branches. Mol. Cell. Neurosci. *17*, 624–636.

Suter, D.M., and Forscher, P. (1998). An emerging link between cytoskeletal dynamics and cell adhesion molecules in growth cone guidance. Curr. Opin. Neurobiol. *8*, 106–116.

Thurnherr, T., Benninger, Y., Wu, X., Chrostek, A., Krause, S.M., Nave, K.A., Franklin, R.J., Brakebusch, C., Suter, U., and Relvas, J.B. (2006). Cdc42 and Rac1 signaling are both required for and act synergistically in the correct formation of myelin sheaths in the CNS. J. Neurosci. *26*, 10110–10119.

Vitriol, E.A., and Zheng, J.Q. (2012). Growth cone travel in space and time: the cellular ensemble of cytoskeleton, adhesion, and membrane. Neuron *73*, 1068–1081.

Wilson, R., and Brophy, P.J. (1989). Role for the oligodendrocyte cytoskeleton in myelination. J. Neurosci. Res. *22*, 439–448.